Nanostructured $Si_{(1-x)}Ge_x$ for Tunable Thin Film Lithium-Ion Battery Anodes

Paul R. Abel,[†] Aaron M. Chockla,[†] Yong-Mao Lin,[†] Vincent C. Holmberg,[†] Justin T. Harris,[†] Brian A. Korgel,[†,§] Adam Heller,[†] and C. Buddie Mullins[†,‡,§,*]

[†]Departments of Chemical Engineering, [‡]Chemistry and Biochemistry, Center for Electrochemistry, and [§]Texas Materials Institute, University of Texas at Austin, 200 E Dean Keeton Street C0400, Austin, Texas 78712, United States

ABSTRACT Both silicon and germanium are leading candidates to replace the carbon anode of lithium ions batteries. Silicon is attractive because of its high lithium storage capacity while germanium, a superior electronic and ionic conductor, can support much higher charge/discharge rates. Here we investigate the electronic, electrochemical and optical properties of $Si_{(1-x)}Ge_x$ thin films with x = 0, 0.25, 0.5, 0.75, and 1. Glancing angle deposition provided amorphous films of reproducible nanostructure and porosity. The film's composition and physical properties were investigated by X-ray photoelectron spectroscopy, four-point probe conductivity, Raman, and UV—vis absorption spectroscopy. The films were assembled into coin cells to test their electrochemical properties as a lithium-ion battery anode material. The cells were cycled at various C-rates to determine the upper limits for high rate performance. Adjusting the composition in the $Si_{(1-x)}Ge_x$ system demonstrates a trade-off between rate capability and specific capacity. We show that high-capacity silicon anodes and high-rate germanium anodes are merely the two extremes; the composition of $Si_{(1-x)}Ge_x$ alloys provides a new parameter to use in electrode optimization.
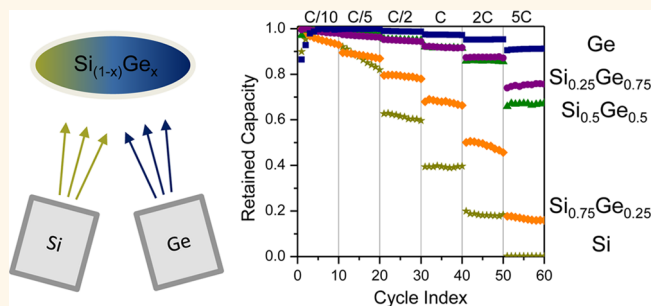
KEYWORDS: silicon · germanium · SiGe · lithium-ion battery · glancing angle deposition

L ithium ion batteries have enabled the widespread adoption of portable electronic devices but their continued development is limited by the electrode chemistries. Currently available cells utilize carbonaceous materials in the anode, but safety concerns as well as a limited capacity—especially at high charge/discharge rates—has led to the search for new, superior anode materials. Alloy type electrodes are a promising class of materials that includes both silicon and germanium. These materials store lithium through the formation of a bulk lithiated alloy and have capacities several times that of graphite. The thermodynamic limits for lithium alloy formation have been found to be $Li_{22}X_5$ (X = Si,Ge) which represents 4200 mAh g^{-1} for Si,[1] and 1624 mAh g^{-1} for Ge[2]; these capacities have been realized at elevated temperatures, but studies on electrochemical lithiation of silicon at room temperature have shown that the highest accessible state is $Li_{15}Si_4$, which still represents a capacity of 3579 mAh g^{-1}.[1,3,4] There is still confusion about the accessible

capacity for germanium. Baggetto et al. reports 1384 mAh g^{-1},[5] corresponding to $Li_{15}Ge_4$, but others report capacities close to 1624 mAh g^{-1} indicative of $Li_{22}Ge_5$.[6] In either case, the capacity is significantly higher than that of the presently used graphitic material.

Silicon has been extensively studied due to its high capacity, low cost, and abundance, with promising results.[7-14] Germanium has also attracted attention due to its favorable electronic conductivity, ionic diffusivity, and capacity.[6,15-21] Germanium's intrinsic electronic conductivity at room temperature is 2.1 S m^{-1}, 3 orders of magnitude higher than that of silicon (1.6 × 10^{-3} S m^{-1}).[22] Additionally, the diffusivity of lithium in germanium is 6.25 × 10^{-12} $cm^2 s^{-1}$, 2 orders of magnitude higher than in silicon (1.9 × 10^{-14} $cm^2 s^{-1}$).[23] However, the high cost and low abundance of germanium are hurdles to its widespread adoption. Both materials share the disadvantage of undergoing large volumetric expansion upon lithiation. Nanostructuring has been shown to prevent

© 2013 American Chemical Society

electrode pulverization in silicon and germanium independently and is expected to work for the alloy system as well. Here we use the term alloy to refer to only the silicon−germanium alloy. Lithium−silicon−germanium ternary compounds will be referred to as lithiated alloys.

Silicon and germanium are miscible over the entire compositional range. Additionally, the compositions of the terminal phases accessible through electrochemical lithiation have identical lithium content, are isostructural, and have similar lattice constants (10.777 Å for $Li_{15}Si_4$[3] and 10.783 Å for $Li_{15}Ge_4$,[24] each with 3.75 mols of lithium per mole of silicon or germanium). Assuming that the alloy is lithiated to $Li_{15}(Si_{(1-x)}Ge_x)_4$, the specific capacity of the alloy should scale with composition according to eq 1.1

$$\text{specific capacity } (mA \cdot h \cdot g^{-1}) = \frac{\xi n F}{(1-x)M_{Si} + x M_{Ge}}$$

where ξ is the extent of reaction reaction (taken to be 3.75 mols of lithium per mole of alloy—this corresponds to the formation of $Li_{15}(Si_{(1-x)}Ge_x)_4$), n is the charge carried by the lithium ion, F is the Faraday constant, x is the mole fraction of germanium in the alloy, and M_{Si} and M_{Ge} are the molar masses of silicon and germanium.

Silicon−germanium alloys have been extensively studied for application to the semiconductor industry. The electrical conductivity of the alloy has been found to vary monotonically with composition between the bounds set by the pure species.[25] The intermediate electrical conductivity of silicon−germanium alloys should increase the high-rate performance of the alloy relative to the silicon baseline. Additionally, the ionic conductivity of lithium in the alloy has been studied at elevated temperatures by Atabaev et al.[26] They found that, despite the higher ionic conductivity of germanium, the ionic conductivity of the alloy decreased with increasing germanium content over the compositional range 0−35 atom % germanium. The trend was accentuated as the temperature was lowered (from 500 °C to 300 °C). The study did not investigate the behavior of alloys with high germanium content, but it would be expected that the ionic conductivity would increase as the composition becomes closer to pure germanium.

Several groups have investigated layered silicon−germanium systems.[27−29] However, alloy systems have not been well studied, and the reported results do not follow the expected trends. Hashimoto et al. used ball milling to create $Li_{4.4}Si_{(1-x)}Ge_x$ powder for use as an active material in all-solid-state batteries.[30] X-ray diffraction showed that the desired phases had been formed, but the material was cycled versus a lithiated cathode ($LiCo_{0.3}Ni_{0.7}O_2$). The authors state that the alloys reach a lithiated phase of $Li_ySi_{(1-x)}Ge_x$ with y ranging from 4.9 to 5.45 depending on the silicon to germanium ratio, but provide no evidence that the additional lithium was incorporated into the lithium−silicon−germanium alloy. Wang et al. investigated $Si_{(1-x)}Ge_x$ sputtered onto a copper nanowire array and found that capacity retention varied with composition, with the most stable composition being $Si_{0.6}Ge_{0.4}$.[31] Further investigation of the properties of the silicon−germanium alloys was limited to this composition, so the changes in the electrochemical properties with material composition could not be tracked. Our results show a different trend in how capacity retention varies with composition; however, this could be due to differences in the deposition techniques or substrate materials (and hence film adhesion).

In this work we synthesize nanostructured amorphous thin films by glancing angle deposition (GLAD). GLAD is a physical vapor deposition technique where the adatoms are directed at the substrate at high angles of incidence. In the early stages of deposition stochastic variations in deposition rate lead to surface roughening. The roughness is amplified by self-shadowing leading to the growth of nanocolumnar films. We employ multiple independently controlled evaporators to coevaporate silicon and germanium. Additional details regarding this technique are described elsewhere.[32−37] We vary the mole fraction of germanium in the alloy from 0 to 1. We show that the electronic conductivity increases with increasing germanium content and that the high-rate performance of the alloy increases with increasing germanium content, but the specific capacity decreases with increasing germanium content. These opposing trends provide application specific optimal compositions based on the needed specific capacity, C-rate performance, and material cost.

RESULTS AND DISCUSSION

Material Characterization. SEM images of $Si_{(1-x)}Ge_x$ films deposited with an incident angle of 70° from surface normal are shown in Figure 1. The films are nanocolumnar over the entire compositional range, but the feature size increases slightly with increasing germanium content. The column diameter is ∼10 nm for the silicon film, but the diameter has increased to ∼20 nm for the pure germanium film. As the germanium content increases the morphology changes: the individual columns become smoother, that is, they have fewer branches. This is likely due to germanium's lower melting point. As a general rule, nanostructuring can only be achieved if the substrate temperature is less than 30% of the material's melting point.[33] As the germanium content is increased, it becomes more difficult to grow the nonequilibrium nanocolumnar structures. Because there are morphological changes associated with the changes in composition, we cannot rigorously attribute all changes in electrochemical behavior to compositional effects, but the degree of
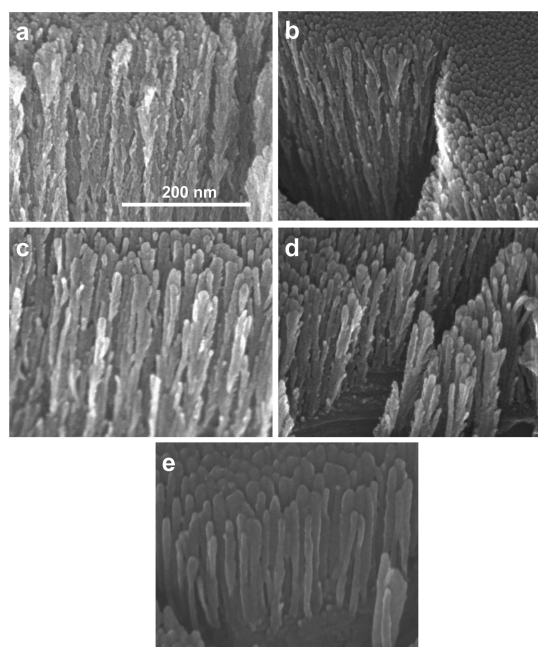
Figure 1. SEM Images of (a) Si, (b) $Si_{0.75}Ge_{0.25}$, (c) $Si_{0.5}Ge_{0.5}$, (d) $Si_{0.25}Ge_{0.25}$, (e) Ge thin films deposited at 70° from normal. The scale bar in panel a applies to all images.

change in morphology is small compared to the degree of change in measured material properties, so we attribute a majority of the electrochemical changes to changes in composition.

GLAD synthesis of high melting point materials has been shown to result in amorphous films, and in the case of multicomponent depositions, the compositions have been shown to be well mixed.[34,37] The ability to grow nonequilibrium, nanocolumnar structures requires that surface diffusion of adatoms be limited. In contrast, phase segregation and crystallization require some degree of surface mobility during deposition to allow for energetically favorable order to develop. No X-ray diffraction peaks were observed for any of the as deposited films. High-resolution transmission electron microscope (HRTEM) imaging and energy-dispersive X-ray spectroscopy (EDS) was performed to ensure that the as deposited material was both amorphous and well mixed. Figure 2a shows the HRTEM image of an individual $Si_{0.25}Ge_{0.75}$ nanocolumn. There are no observable lattice fringes indicating that the material is, in fact, amorphous. An EDS line-scan was performed along the path indicated by the arrow in Figure 2a. The intensity of the silicon and germanium k_α transitions along that path are shown in Figure 2b. The line-scan shows that there are no spacial inhomogenaities in the composition. This confirms that the films are well mixed. Additionally, the film composition as measured by EDS was $Si_{0.26}Ge_{0.74}$, in good agreement with the nominal value determined by the silicon to germanium flux ratio during deposition.

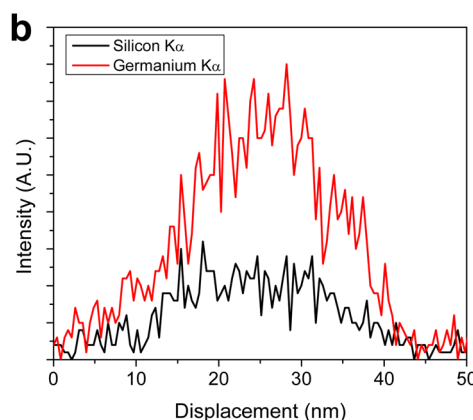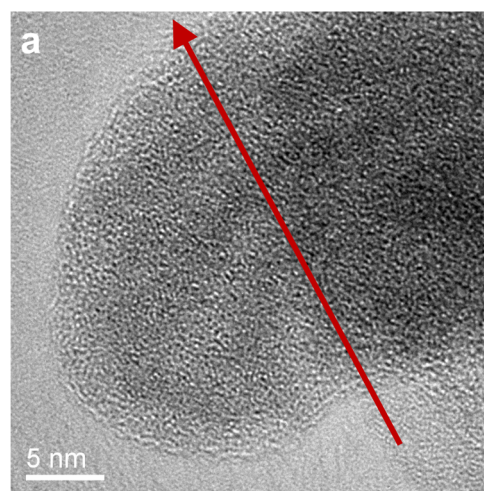Figure 3 shows the Si 2p and Ge 3d peaks of the X-ray photoelectron spectra for the $Si_{(1-x)}Ge_x$ films. The

Figure 2. (a) HRTEM image of a single $Si_{0.25}Ge_{0.75}$ nanocolumn; (b) EDS line-scan across the nanocolumn.

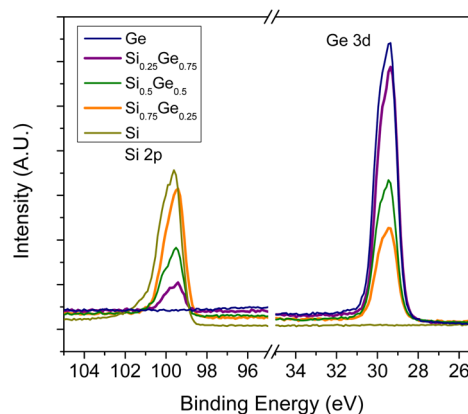**Figure 3.** XPS spectra of dense $Si_{(1-x)}Ge_x$ films. Quantitative analysis of the Si 2p and Ge 3d peaks indicated that the composition of the films was within a few percentage points of the nominal values. The measurements were repeated at various depths in the films with no change in measured composition.

integrated areas of the peaks are used to confirm the nominal compositions of the films determined by the silicon and germanium fluxes measured during deposition. The compositions did not vary upon sputtering, that is, as a function of depth and matched the nominal
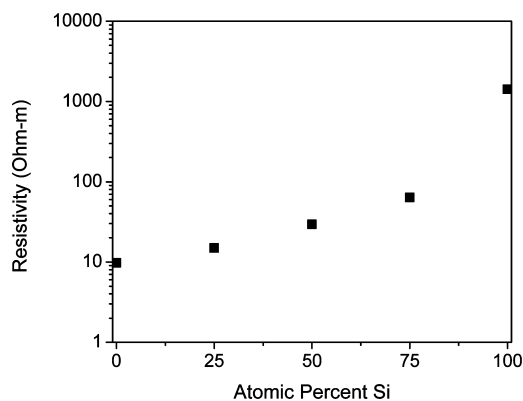
Figure 4. Electrical resistivities of dense Si$_{(1-x)}$Ge$_x$ thin films measured using a four-point probe.

Figure 5. Raman spectra of (a) as deposited and (b) Raman-laser annealed Si$_{(1-x)}$Ge$_x$ films.

Figure 6. Absorptance spectra of Si$_{(1-x)}$Ge$_x$ films.

compositions within a few percent. The measured compositions of the alloy films were Si$_{0.75}$Ge$_{0.25}$, Si$_{0.48}$Ge$_{0.52}$, and Si$_{0.22}$Ge$_{0.78}$. The silicon and germanium films were found to be free of measurable contaminants.

Figure 4 shows the electrical resistivity of dense Si$_{(1-x)}$Ge$_x$ films deposited on glass at normal incidence. In each case, the resistivity is significantly lower than the intrinsic values published for that composition. The resistivity of semiconductors, however, is very sensitive to impurities. In the manufacture of electronic devices, in the context of which the earlier values were measured, the purity is at least 99.9999%. In contrast, technical grade materials with 99.999% purity were used as the evaporation sources rather than the higher purity semiconductor grade materials. Lower purity could be responsible for the lower than intrinsic resistivity values if the impurities act as n- or p-type dopants rather than midgap states. While the level of impurities is still far below the detection limit for XPS, it is enough to have a significant effect on the resistivity of the films. The lower resistivity of the materials is beneficial to the electrochemical performance of the electrodes, especially at high charge rates.

The resistivity fell by nearly 2 orders of magnitude when 25 atom % germanium was incorporated in Si. As the fraction of germanium was increased further, the resistivity slowly fell to the value for pure germanium, that is, the incremental drop in resistivity was largest for small germanium mole fractions. This indicates that a large benefit in electrical resistivity can be gained without sacrificing a large fraction of silicon's capacity.

Raman spectra of the dense Si$_{(1-x)}$Ge$_x$ films deposited on glass at normal incidence were measured. The spectra from the as deposited films are shown in Figure 5a. The features are diffuse as well as shifted $\sim$30 cm^{-1} lower than the expected values for the pure crystalline materials (521 cm^{-1} for Si and 298 cm^{-1} for Ge). Both of these indicate that the material is amorphous. Broad peaks characteristic of Si—Si, Si—Ge, and Ge—Ge vibrations are present for the intermediate
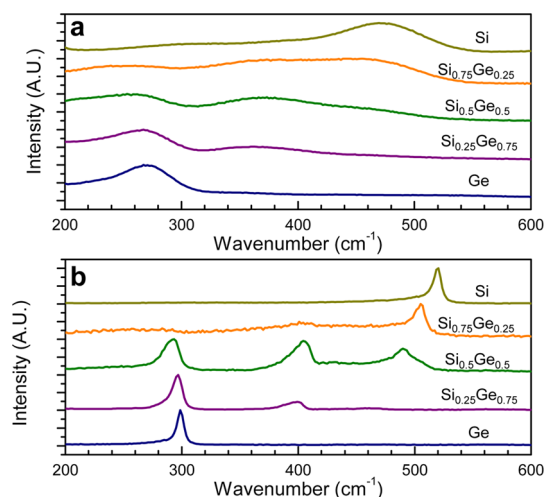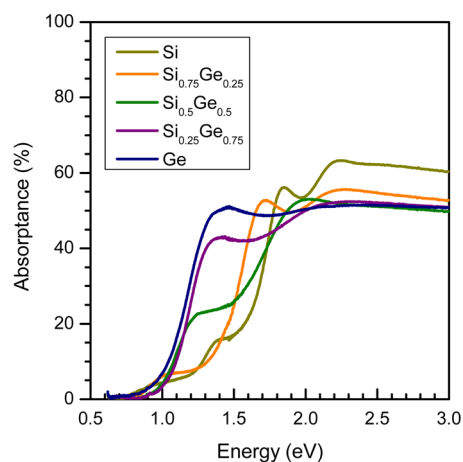
compositions. The features sharpen considerably after annealing the films with the Raman laser. Spectra of annealed films are shown in Figure 5b. Expectedly, the pure silicon and pure germanium films show only vibrations of the homogeneous bonds, whereas the Si—Ge vibration is observed in the intermediate compositions. The peak intensities of the Si—Si, Si—Ge, and Ge—Ge vibrations are similar in the Si$_{0.5}$Ge$_{0.5}$ film, consistent with random bonding of silicon and germanium rather than preferred bonding of Si with Si or of Ge with Ge. The Si$_{0.75}$Ge$_{0.25}$ and Si$_{0.25}$Ge$_{0.75}$ films each had a strong peak for the majority component homogeneous bond and a minor peak for the heterogeneous bond. Additionally, the Si—Si peak shifts to lower wavenumbers as the germanum content of the film is increased. This is due to the germanium atoms disrupting the silicon lattice. The reciprocal is also true. The Ge—Ge peak shifts to lower wavenumbers as the silicon content of the films increases.

Figure 6 shows absorptance measurements made on dense Si$_{(1-x)}$Ge$_x$ films deposited on glass at normal

incidence. The band gap of a-Si is expected at 1.7 eV, however the band edge appears to start as low as 0.8 eV. Furthermore, there are multiple features in the Si spectrum. A shoulder begins between 1.1 and 1.2 eV, which corresponds to the band gap of c-Si. The curve steepens again around 1.6 eV to a peak centered at 1.8 eV near the value for the band gap of a-Si. Yet another peak begins around 2.0 eV which corresponds to the E_L transition in Si. The reason for the enhanced absorptance at low energies remains unclear, as the HRTEM measurements indicate that the as deposited material is perfectly amorphous. Data from the electrochemical tests performed on this material are characteristic of a-Si, as well.

The pure Ge spectrum shows a band edge near the expected value of 0.67 eV. The absorptance begins at this point and increases monotonically to a value of ∼50%, then levels off. There is a shallow peak centered around 1.2 eV that corresponds to the E_X transition in Ge. The absorption is expected to blueshift with increasing Si content.[38] However, the band edge for the intermittent $Si_{(1-x)}Ge_x$ compounds does not deviate from that of the Ge spectrum, and the Ge E_X transition peak location remains nearly constant as the composition is changed from Ge to $Si_{0.5}Ge_{0.5}$ with the only difference being the relative absorptance. This indicates a lack of compositional homogeneity at the atomic level—the $Si_{(1-x)}Ge_x$ materials synthesized in this study are disordered alloys rather than ordered intermetallics. The Raman data are also somewhat indicative of this feature, which becomes evident when examining the $Si_{0.5}Ge_{0.5}$ film. In an ordered film, the Si—Ge stretch is the only expected peak, as every Si atom would be bonded to a Ge atom, and vice versa. The Si—Si and Ge—Ge stretches are still observed, however. In fact, the Ge—Ge stretch is evident in the Ge, $Si_{0.25}Ge_{0.75}$ and $Si_{0.5}Ge_{0.5}$ Raman spectra. The band edge for these films remains at the expected value for pure Ge. The $Si_{0.75}Ge_{0.25}$ Raman spectrum is dominated by the Si—Si stretch and shows little Si—Ge or Ge—Ge bonding.

Electrochemical Testing. The results of charge/discharge cycling at rates up to 20C are shown in Figure 7a. The reversible capacity of the pure silicon film is 2640 mAh g^{-1}, which is lower than theoretical, but consistent with our previous results for silicon films.[9] The capacities of the $Si_{0.75}Ge_{0.25}$, $Si_{0.5}Ge_{0.5}$, $Si_{0.25}Ge_{0.75}$, and Ge films are 2121, 1883, 1652, and 1217 mAh g^{-1}, respectively. These values are lower than expected on the basis of the weighted combination of the capacities of the alloy's components. Specific capacity values were sensitive to the extent of surface oxidation. The films used in this study were exposed to air for 72 h before assembly into coin cells to allow the formation of a terminal native oxide layer. Additional films with minimum exposure to atmosphere between deposition and coin cell assembly showed capacities much
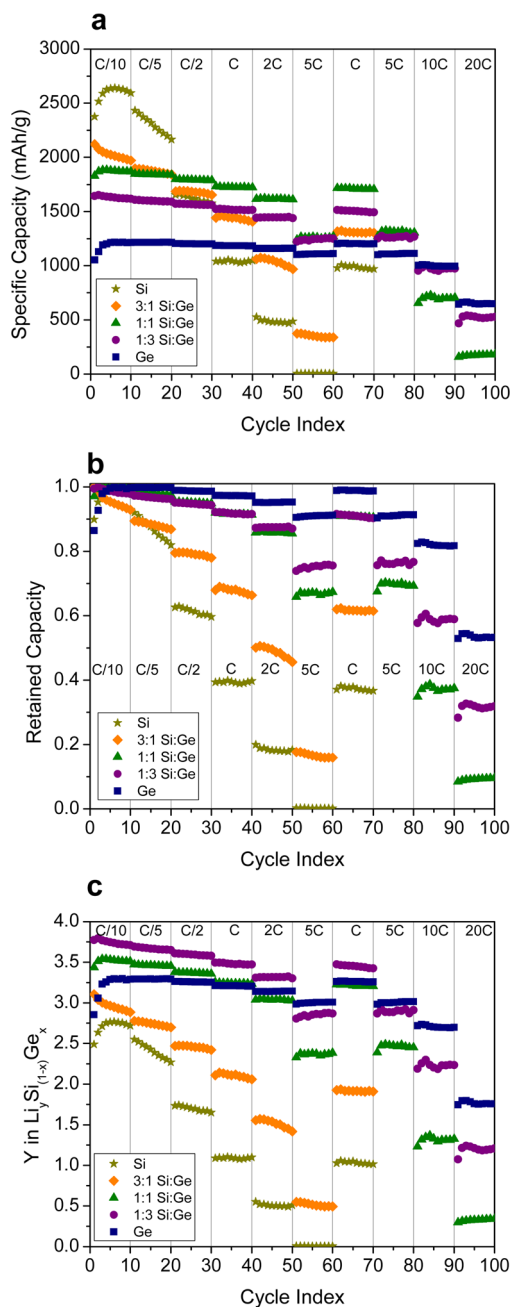

Figure 7. Cycling data of films. (a) Specific capacity, (b) retained capacity, and (c) lithium content. Data for pure Si and $Si_{0.75}Ge_{0.25}$ are not shown for cycles 70−100 because the materials could not support the high charge/discharge rates.

closer to expected values, see Supporting Information, Figures S1−S5. Returning to the data displayed in Figure 7, as the C-rate is increased, the performance of the films decreases with pure silicon degrading the most and pure germanium the least. The capacity of the silicon electrode is nearly zero at 5C. After cycling at 5C, the rate is decreased to 1C in order to determine the extent that the capacities recover. All of the compositions show good capacity recovery. After the recovery cycles, cycling of the $Si_{0.5}Ge_{0.5}$, $Si_{0.25}Ge_{0.75}$, and Ge electrode was continued at 5C, 10C, and then 20C

rates. The germanium electrode retained a capacity of 644 mAh g^{-1} at 20C, over half of its C/10 capacity. Figure 7b shows the cycling data normalized to the maximum capacity of each material. Germanium retains the highest percentage of initial capacity at high rates; this is attributed to its high electronic and ionic conductivities. The retained capacity of the various alloys at a given C-rate decreases with decreasing germanium content; this is a reflection of the conductivity decreasing along with the germanium content. Figure 7c shows the same data presented in terms of moles of lithium stored per mole of alloy. Equation 1.1 assumed that each composition could store an equal 3.75 mols of lithium per mole of alloy, but this is not the case. The reversible lithium storage at low currents ranges from 2.75 for silicon to 3.75 for $Si_{0.25}Ge_{0.75}$. The extent of lithiation does not appear to be limited by charge transport or ionic diffusion, as germanium, the material with the highest capacity retention at high rates has an intermediate lithium storage capacity on a molar basis. Additionally, the trend does not appear to be mediated by expansion-induced structural damage as silicon shows the largest capacity fade while having the lowest molar lithium storage capacity. At this point the reason for the differences in molar lithium storage capacity remains unclear.

The voltage profiles for the first two cycles for each composition are shown in Figure 8. The behavior of the films can be split into three groups, with Si and $Si_{0.75}Ge_{0.25}$ forming a group of silicon-like materials; $Si_{0.5}Ge_{0.5}$ exhibiting intermediate behavior; and $Si_{0.25}Ge_{0.75}$ and Ge forming a group of germanium-like materials. The silicon-like materials exhibit two broad lithium insertion and extraction pseudoplateaus, these pseudoplateaus are characteristic of single-phase lithiation where the lithium electrochemical potential in the host alloy is changing with composition as additional lithium is added. The germanium-like materials exhibit two lithium insertion pseudoplateaus, but a single lithium extraction plateau. This single plateau is characteristic of a two-phase coexistence lithium deinsertion mechanism.

Additional insight into the separation of lithiation behaviors into distinct groups is obtained by looking at the voltage profiles in differential form as shown in Figure 9. The potential of the lithiation and delithiation features varies significantly with composition. During lithiation, each material exhibits broad features characteristic of single-phase lithiation of an amorphous material. However the features shift to more positive potentials as the mole fraction of germanium is increased. For pure silicon, the two broad lithiation features are at ~60 and ~220 mV. For germanium, these peaks are at ~170 mV and ~370 mV. A third peak at ~510 mV is also present. No third peak is present in silicon. This is consistent with previous reports in the literature.[3,5] For the alloys, the position of the two lithiation features varies linearly with composition
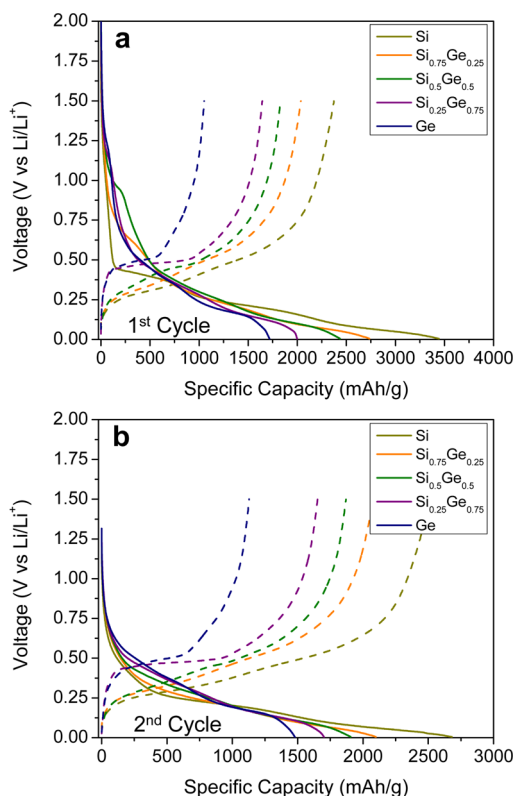

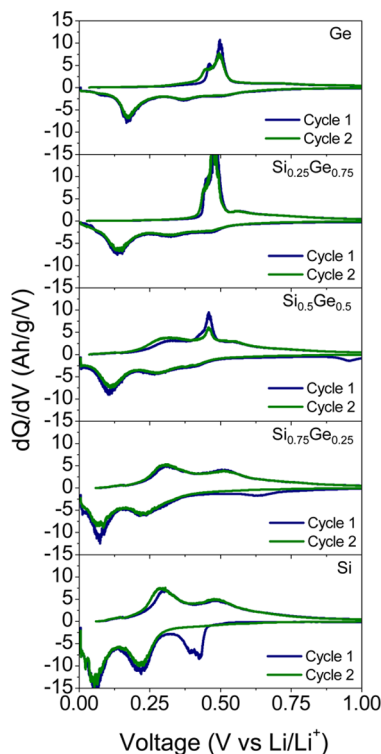Figure 8. Voltage profiles for the (a) first and (b) second charge/discharge cycles of $Si_{(1-x)}Ge_x$ electrodes.

Figure 9. Differential capacity plots for the first and second cycles of $Si_{(1-x)}Ge_x$ films.

between the two extreme voltages set by the pure components. Additionally, the third germanium peak
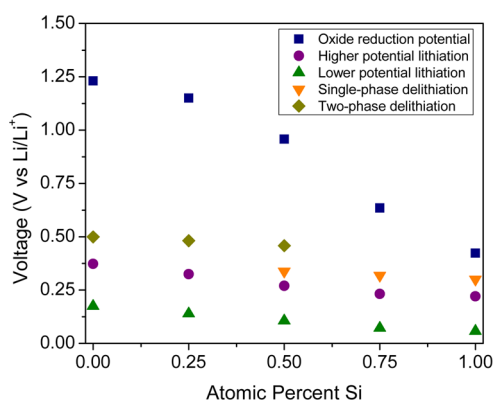
Figure 10. Dependence of the peak potentials for lithium insertion and deinsertion on material composition.

grows in as the germanium content is increased. The peak potentials for the first cycle lithiation features of the various alloys are plotted in Figure 10. The fact that the alloys exhibit shifts in peak position rather than multiple peaks corresponding to pure silicon and pure germanium is additional evidence that the alloys are well mixed at the atomic level.

The lithium extraction behavior of silicon and germanium are markedly different. Silicon undergoes a single-phase delithiation indicated by two broad oxidation features while germanium exhibits one very sharp feature indicating a two-phase mechanism. The silicon-like single-phase behavior of the $Si_{0.75}Ge_{0.25}$ alloy and the germanium-like two-phase behavior of the $Si_{0.25}Ge_{0.75}$ alloys are clearly visible, and the $Si_{0.5}Ge_{0.5}$ alloy shows a superposition of the two behaviors with a sharp germanium-like delithiation feature growing out of the two broad silicon-like features. Baggetto et al. showed that this single lithium extraction peak in pure germanium resulted from the crystallization of lithiated germanium into the $Li_{15}Ge_4$ phase at potentials below 110 mV.[5] The presence of this feature in the germanium-like materials indicates similar behavior. Silicon has been known to crystallize into the $Li_{15}Si_4$ phase when lithiated to potentials below 50 mV; however, the phenomenon is particle-size dependent, and some morphologies do not crystallize even when held at 0 V.[3] Germanium undergoes crystallization at more positive potentials, thus enabling the formation of the crystalline phase. A small peak is observed at 85 mV for germanium and at 65 mV for $Si_{0.25}Ge_{0.75}$ that we attribute to the crystallization into the $Li_{15}(Si_{(1-x)}Ge_x)_4$ phase. This is analogous to the feature

reported by Baggetto et al.[5] Similar peaks are not present in the films with higher silicon content; most likely due to the more negative voltages required to form the crystalline phase in these films. We believe that the intermediate behavior of $Si_{0.5}Ge_{0.5}$ is due to the material being only partially crystallized at the lower cutoff voltage in the test. These differences can explain the fundamentally different behaviors of the silicon-like and germanium-like materials. Additionally, the lithium deinsertion peaks shift with material composition. The sharp two-phase coexistence peak shifts from 460 mV in $Si_{0.5}Ge_{0.5}$ to 500 mV in pure germanium. The broad single-phase deinsertion peak shifts from 300 mV in pure silicon to 340 mV in $Si_{0.5}Ge_{0.5}$.

For pure silicon, there is another peak at ~400 mV which is attributed to the reaction of lithium with surface oxide.[9] Additional information on these oxide reduction peaks can be found in the Supporting Information. There is an analogous feature in the alloys and in the pure germanium film that shifts to higher voltages as germanium content is increased. This shift is also nearly linear with composition. The magnitude of the oxide reduction feature also decreases with increasing germanium content. This is consistent with the native oxide layer that forms on germanium being thinner than what forms on silicon. The shift in the oxide-reduction potential as a function of composition is also shown in Figure 10.

CONCLUSIONS

Silicon−germanium alloys of different compositions offer a range of high rate (up to 20C) and high specific capacity lithium-ion battery anodes. The electronic conductivity increases while the specific capacity decreases as germanium content is increased. Additionally, the high-rate performance of the material increases substantially with increasing germanium content. While the silicon films in this study retained almost zero capacity when cycled at 5C, the germanium films retained ~90% their initial capacity, $Si_{0.25}Ge_{0.75}$ retained ~75%, and $Si_{0.5}Ge_{0.5}$ retained ~68%. Silicon alloying mitigates the high cost of germanium and increases the specific capacity of the material. These benefits can outweigh the loss of high rate performance—particularly if the maximum charge/discharge rate for the cell is below 5C. $Si_{(1-x)}Ge_x$ alloys give an additional parameter to adjust when tailoring the anode material to the specific current densities demanded by a given battery application.

MATERIALS AND METHODS

Material Synthesis. Thin films of $Si_{(1-x)}Ge_x$ were synthesized in high vacuum ($< 1 \times 10^{-7}$ Torr) by evaporative deposition at normal or glancing angles. Total film mass densities of 50 μg cm^{-2} were used which corresponds to dense film thicknesses of 94, 109, 130, 162, and 215 nm for Ge, $Si_{0.25}Ge_{0.75}$, $Si_{0.5}Ge_{0.5}$, $Si_{0.75}Ge_{0.25}$, and Si, respectively. Silicon shot (99.999% Alfa Aesar) was evaporated using a Telemark 118 electron beam

evaporator, and germanium was evaporated using a custom-built electron beam evaporator. The evaporators are operated independently with both evaporants directed at the center of the vacuum chamber. Each deposition rate could be individually controlled and independently measured using a quartz crystal microbalance (inficon SQM-160 with cool-drawer sensor feedthrough). The silicon deposition rate was monitored throughout the entire deposition, while the germanium

deposition rate was measured before and after deposition. Variation in the germanium deposition rate between the two measurements was less than 10%. Films for electrochemical testing were deposited on 15.8 mm, 300 series stainless steel disks (MTI Corp.), and films for *ex-situ* analysis were deposited on glass slide covers (Fisher Scientific). The substrate was mounted on a rotary probe, allowing the deposition angle to be adjusted between 0° and 90° (between surface normal and parallel).

Material Characterization. Imaging of the as deposited films was performed using a Hitachi S5500 in SEM mode with an acceleration voltage of 20 kV. The composition was measured by XPS using a commercial X-ray photoelectron spectrometer (Kratos Axis Ultra), utilizing a monochromatic Al−Kα X-ray source (hν = 1486.5 eV). An automated charge neutralizer was employed for analysis. Casa XPS analysis software was used to determine the stoichiometry of samples from corrected peak areas, employing Kratos sensitivity factors for each element of interest. Electrical conductivity was measured using a Lucas 302 four-point probe with a Keithly 220 programmable current source.

Raman spectroscopy was performed using a Renishaw inVia microscope equipped with a 514.5 nm argon ion laser in backscattering configuration. The Stokes Raman signal at 521 cm^{-1} for single-crystalline bulk Si oriented with the [110] direction normal to the laser was used to calibrate the instrument. The beam was focused using an optical microscope with a 50× objective lens. Spectra were taken on SiGe films deposited on glass slides by single scans at 5% laser power (0.2 mW). The films were annealed using 100% laser power to induce local crystallization, and spectra were taken again on the SiGe films using 5% laser power.

Absorptance measurements were made using a Cary 500 UV−vis−NIR spectrophotometer attached to a Labsphere DRA-CA-5500 integrating sphere. Samples were suspended in the center of the integrating sphere using a clip-style center mount, and the total transmitted and reflected light were measured simultaneously. This transmittance + reflectance (transflectance) measurement gives the net percentage of light transmitted through and reflected by the sample ($T + R$). The absorptance (A) of the sample is then given by eq 2.2

$$A = 100\% - (T + R)$$

Electrochemical Testing. Samples were removed from the deposition chamber and exposed to atmosphere for 72 h prior to being assembled into coin cells inside a glovebox (MBraun Unilab). This allowed for the formation of a native oxide layer on the surface of the films. Substrates were assembled into type 2032 coin cells against a lithium metal (Alfa Aesar 99%) counter/reference electrode. The electrolyte was 1 M LiPF6 in FEC/DEC 1:1 (FEC from Solvay Chemicals). Several studies have shown that FEC-based electrolytes promote stable cycling with silicon and germanium electrodes.[13,21,39−41] A 25 μm thick polypropylene film separator (Celgard 2400) was used. After assembly into coin cells, the electrochemical behavior of samples was tested on a multichannel battery tester (Arbin BT2143). Cells were cycled between 5 mV and 1.5 V at various currents with a 5 min rest period between charge/discharge half cycles. Films were tested for 10 cycles at C/10 followed by 10 cycles each at C/5, C/2, C, 2C, 5C, and then a final 10 cycles at C/10 to examine how the samples recovered from the high rate tests. The cells that performed well at 5C were subjected to an additional 30 cycles with 10 cycles each at 5C, 10C, and 20C. C-rates were calculated for each composition based on eq 1.

Conflict of Interest: The authors declare no competing financial interest.

Supporting Information Available: Additional figures and text detailing the differences in electrochemical behavior between pristine samples and those with a native oxide. This material is available free of charge *via* the Internet at http://pubs.acs.org.

REFERENCES AND NOTES

1. Wen, C. J.; Huggins, R. A. Chemical Diffusion in Intermediate Phases in the Lithium−Silicon System. *J. Solid State Chem.* **1981**, *37*, 271–278.
2. St. John, M. R.; Furgala, A. J.; Sammells, A. F. Thermodynamic Studies of Li-Ge Alloys: Application to Negative Electrodes for Molten Salt Batteries. *J. Electrochem. Soc.* **1982**, *129*, 246–250.
3. Hatchard, T. D.; Dahn, J. R. *In Situ* XRD and Electrochemical Study of the Reaction of Lithium with Amorphous Silicon. *J. Electrochem. Soc.* **2004**, *151*, A838–A842.
4. Obrovac, M. N.; Christensen, L. Structural Changes in Silicon Anodes during Lithium Insertion/Extraction. *Electrochem. Solid-State Lett.* **2004**, *7*, A93–A96.
5. Baggetto, L.; Notten, P. H. L. Lithium-Ion (De)Insertion Reaction of Germanium Thin-Film Electrodes: An Electrochemical and *in Situ* XRD Study. *J. Electrochem. Soc.* **2009**, *156*, A169–A175.
6. Graetz, J.; Ahn, C. C.; Yazami, R.; Fultz, B. Nanocrystalline and Thin Film Germanium Electrodes with High Lithium Capacity and High Rate Capabilities. *J. Electrochem. Soc.* **2004**, *151*, A698–A702.
7. Zhou, S.; Liu, X.; Wang, D. Si/TiSi$_2$ Heteronanostructures as High-Capacity Anode Material for Li Ion Batteries. *Nano Lett.* **2010**, *10*, 860–863.
8. Magasinski, A.; Dixon, P.; Hertzberg, B.; Kvit, A.; Ayala, J.; Yushin, G. High-Performance Lithium-Ion Anodes Using a Hierarchical Bottom-Up Approach. *Nat. Mater.* **2010**, *9*, 353–358.
9. Abel, P. R.; Lin, Y.-M.; Celio, H.; Heller, A.; Mullins, C. B. Improving the Stability of Nanostructured Silicon Thin Film Lithium-Ion Battery Anodes through Their Controlled Oxidation. *ACS Nano* **2012**, *6*, 2506–2516.
10. Chan, C. K.; Patel, R. N.; O'Connell, M. J.; Korgel, B. A.; Cui, Y. Solution-Grown Silicon Nanowires for Lithium-Ion Battery Anodes. *ACS Nano* **2010**, *4*, 1443–1450.
11. Chan, C. K.; Peng, H.; Liu, G.; McIlwrath, K.; Zhang, X. F.; Huggins, R. A.; Cui, Y. High-Performance Lithium Battery Anodes Using Silicon Nanowires. *Nat. Nanotechnol.* **2008**, *3*, 31–35.
12. Fleischauer, M. D.; Li, J.; Brett, M. J. Columnar Thin Films for Three-Dimensional Microbatteries. *J. Electrochem. Soc.* **2009**, *156*, A33–A36.
13. Chockla, A. M.; Klavetter, K.; Mullins, C. B.; Korgel, B. A. Tin-Seeded Silicon Nanowires for High Capacity Li-Ion Batteries. *Chem. Mater.* **2012**, *24*, 3738–3745.
14. Chockla, A. M.; Bogart, T. D.; Hessel, C. M.; Klavetter, K. C.; Mullins, C. B.; Korgel, B. A. Influences of Gold, Binder and Electrolyte on Silicon Nanowire Performance in Li-Ion Batteries. *J. Phys. Chem. C* **2012**, *116*, 18079–18086.
15. Chan, C. K.; Zhang, X. F.; Cui, Y. High Capacity Li Ion Battery Anodes Using Ge Nanowires. *Nano Lett.* **2007**, *8*, 307–309.
16. Chockla, A. M.; Panthani, M. G.; Holmberg, V. C.; Hessel, C. M.; Reid, D. K.; Bogart, T. D.; Harris, J. T.; Mullins, C. B.; Korgel, B. A. Electrochemical Lithiation of Graphene-Supported Silicon and Germanium for Rechargeable Batteries. *J. Phys. Chem. C* **2012**, *116*, 11917–11923.
17. Laforge, B.; Levan-Jodin, L.; Salot, R.; Billard, A. Study of Germanium as Electrode in Thin-Film Battery. *J. Electrochem. Soc.* **2008**, *155*, A181–A188.
18. Liu, X. H.; Huang, S.; Picraux, S. T.; Li, J.; Zhu, T.; Huang, J. Y. Reversible Nanopore Formation in Ge Nanowires during Lithiation−Delithiation Cycling: An *in Situ* Transmission Electron Microscopy Study. *Nano Lett.* **2011**, *11*, 3991–3997.
19. Park, M.-H.; Cho, Y.; Kim, K.; Kim, J.; Liu, M.; Cho, J. Germanium Nanotubes Prepared by Using the Kirkendall Effect as Anodes for High-Rate Lithium Batteries. *Angew. Chem., Int. Ed.* **2011**, *50*, 9647–9650.

20. Seo, M.-H.; Park, M.; Lee, K. T.; Kim, K.; Kim, J.; Cho, J. High Performance Ge Nanowire Anode Sheathed with Carbon for Lithium Rechargeable Batteries. *Energy Environ. Sci.* **2011**, *4*, 425–428.

21. Chockla, A. M.; Klavetter, K. C.; Mullins, C. B.; Korgel, B. A. Solution-Grown Germanium Nanowire Anodes for Lithium-Ion Batteries. *ACS Appl. Mater. Interfaces* **2012**, *4*, 4658–4664.

22. Conwell, E. M. Properties of Silicon and Germanium. *Proc. Inst. Radio Eng.* **1952**, *40*, 1327–1337.

23. Fuller, C. S.; Severiens, J. C. Mobility of Impurity Ions in Germanium and Silicon. *Phys. Rev.* **1954**, *96*, 21–24.

24. Johnson, Q.; Smith, G. S.; Wood, D. The Crystal Structure of $Li_{15}Ge_4$. *Acta Crystallogr.* **1965**, *18*, 131–132.

25. Levinshtein, M. E. R., Sergey, L.; Shur, Michael, S. *Properties of Advanced Semiconductor Materials: GaN, AlN, InN,NB, SiC, SiGe*; John Wiley and Sons: New York, 2001.

26. Atabaev, I.; Matchanov, N.; Bakhranov, É. Low-Temperature Diffusion of Lithium in Silicon−Germanium Solid Solutions. *Phys. Solid State* **2001**, *43*, 2234–2236.

27. Hwang, C.-M.; Lim, C.-H.; Park, J.-W. Evaluation of Si/Ge Multi-layered Negative Film Electrodes Using Magnetron Sputtering for Rechargeable Lithium Ion Batteries. *Thin Solid Films* **2011**, *519*, 2332–2338.

28. Hwang, C.-M.; Park, J.-W. Electrochemical Properties of Si-Ge-Mo Anode Composite Materials Prepared by Magnetron Sputtering for Lithium Ion Batteries. *Electrochim. Acta* **2011**, *56*, 6737–6747.

29. Song, T.; Cheng, H.; Choi, H.; Lee, J.-H.; Han, H.; Lee, D. H.; Yoo, D. S.; Kwon, M.-S.; Choi, J.-M.; Doo, S. G.; *et al*. Si/Ge Double-Layered Nanotube Array as a Lithium Ion Battery Anode. *ACS Nano* **2012**, *6*, 303–309.

30. Hashimoto, Y.; Machida, N.; Shigematsu, T. Preparation of $Li_{4.4}Ge_xSi_{1-x}$ Alloys by Mechanical Milling Process and Their Properties as Anode Materials in All-Solid-State Lithium Batteries. *Solid State Ionics* **2004**, *175*, 177–180.

31. Wang, J.; Du, N.; Zhang, H.; Yu, J.; Yang, D. $Cu-Si_{1-x}Ge_x$ Core−Shell Nanowire Arrays as Three-Dimensional Electrodes for High-Rate Capability Lithium-Ion Batteries. *J. Power Sources* **2012**, *208*, 434–439.

32. Flaherty, D. W.; Hahn, N. T.; May, R. A.; Berglund, S. P.; Lin, Y.-M.; Stevenson, K. J.; Dohnalek, Z.; Kay, B. D.; Mullins, C. B. Reactive Ballistic Deposition of Nanostructured Model Materials for Electrochemical Energy Conversion and Storage. *Acc. Chem. Res.* **2012**, *45*, 434–443.

33. Hawkeye, M. M.; Brett, M. J. Glancing Angle Deposition: Fabrication, Properties, and Applications of Micro- and Nanostructured Thin Films. *J. Vac. Sci. Technol., A* **2007**, *25*, 1317–1335.

34. Lin, Y.-M.; Abel, P. R.; Flaherty, D. W.; Wu, J.; Stevenson, K. J.; Heller, A.; Mullins, C. B. Morphology Dependence of the Lithium Storage Capability and Rate Performance of Amorphous TiO_2 Electrodes. *J. Phys. Chem. C* **2011**, *115*, 2585–2591.

35. Berglund, S. P.; Rettie, A. J. E.; Hoang, S.; Mullins, C. B. Incorporation of Mo and W into Nanostructured $BiVO_4$ Films for Efficient Photoelectrochemical Water Oxidation. *Phys. Chem. Chem. Phys.* **2012**, *14*, 7065–7075.

36. Berglund, S. P.; Flaherty, D. W.; Hahn, N. T.; Bard, A. J.; Mullins, C. B. Photoelectrochemical Oxidation of Water Using Nanostructured $BiVO_4$ Films. *J. Phys. Chem. C* **2011**, *115*, 3794–3802.

37. Hahn, N. T.; Mullins, C. B. Photoelectrochemical Performance of Nanostructured Ti- and Sn-Doped $\alpha-Fe_2O_3$ Photoanodes. *Chem. Mater.* **2010**, *22*, 6474–6482.

38. Braunstein, R.; Moore, A. R.; Herman, F. Intrinsic Optical Absorption in Germanium−Silicon Alloys. *Phys. Rev.* **1958**, *109*, 695–710.

39. Nakaiz, H.; Kubota, T.; Kita, A.; Kawashima, A. Investigation of the Solid Electrolyte Interphase Formed by Fluoroethylene Carbonate on Si Electrodes. *J. Electrochem. Soc.* **2011**, *158*, A798–A801.

40. Lin, Y.-M.; Klavetter, K. C.; Abel, P. R.; Davy, N. C.; Snider, J. L.; Heller, A.; Mullins, C. B. High Performance Silicon Nanoparticle Anode in Fluoroethylene Carbonate-Based Electrolyte for Li-Ion Batteries. *Chem. Commun.* **2012**, *48*, 7268–7270.

41. Etacheri, V.; Haik, O.; Goffer, Y.; Roberts, G. A.; Stefan, I. C.; Fasching, R.; Aurbach, D. Effect of Fluoroethylene Carbonate (FEC) on the Performance and Surface Chemistry of Si-Nanowire Li-Ion Battery Anodes. *Langmuir* **2011**, *28*, 965–976.